DC-Link Stability Analysis and Controller Design for the Stacked Polyphase Bridges Converter

Mojgan Nikouie, *Student Member, IEEE*, Oskar Wallmark, *Member, IEEE*, Lebing Jin, *Student Member, IEEE*, Lennart Harnefors, *Senior Member, IEEE*, and Hans-Peter Nee, *Senior Member, IEEE*

***Abstract*—The stacked polyphase bridges (SPB) converter consists of several submodules that all are connected in series to a voltage source. The total dc-link voltage should split in a balanced way among the submodules. This does not always occur inherently. This paper presents an analysis of the capacitor voltage stability for the SPB converter. From the analysis, criteria for stability are derived and three alternatives of a suitable balancing controller are designed. The proposed controller alternatives and their associated stability properties are verified on an experimental setup and by simulation.**

***Index Terms*—Balancing control, dc-link stability, integrated electric drive, modular converter.**

I. Introduction

In recent years, modular and multilevel converters have become popular in different low- and medium-voltage applications [1]–[10]. Applications include drives for electric vehicles (EVs) and hybrid electric vehicles (HEVs) [3]–[5]. Integration of the power converter and the electric machine into one single unit brings several advantages for electric drives. An integrated electric drive generally has less amount of cabling, provides size and weight reduction, and also reduces electromagnetic interference compared to a nonintegrated solution [11].

The stacked polyphase bridges (SPB) converter is a type of modular converter that was introduced recently [5]–[8].The combination of the SPB converter and a fractional concentrated winding machine allows for a very compact integrated electric drive, which is attractive for EVs and HEVs [12].

Fig. 1 shows the SPB converter topology. As illustrated, it is comprised of several submodules that are connected in series. Each submodule is a two-level, three-phase converter with low-voltage components, such as low-voltage metal–oxide–semiconductor field-effect transistors (MOSFETs) with a very high switching frequency (in the range of 100 kHz). This allows the SPB converter to use very small, low-voltage film, or possibly ceramic, capacitors. Consequently, they occupy less space, enabling a compact converter–machine integration.

Manuscript received January 28, 2016; revised March 6, 2016; accepted April 5, 2016. Date of publication April 12, 2016; date of current version November 11, 2016. This work was supported by the Swedish Hybrid Vehicle Centre. Recommended for publication by Associate Editor C. N. M. Ho.

M. Nikouie, O. Wallmark, L. Jin, and H.-P. Nee are with the Department of Electric Power and Energy Systems, KTH Royal Institute of Technology, 114 28 Stockholm, Sweden (e-mail: mojgann@kth.se; owa@kth.se; lebingj@kth.se; hansi@kth.se).

L. Harnefors is with the ABB, Corporate Research, 722 26 Västerås, Sweden (e-mail: lennart.harnefors@se.abb.com).

Color versions of one or more of the figures in this paper are available online at http://ieeexplore.ieee.org.

Digital Object Identifier 10.1109/TPEL.2016.2553129

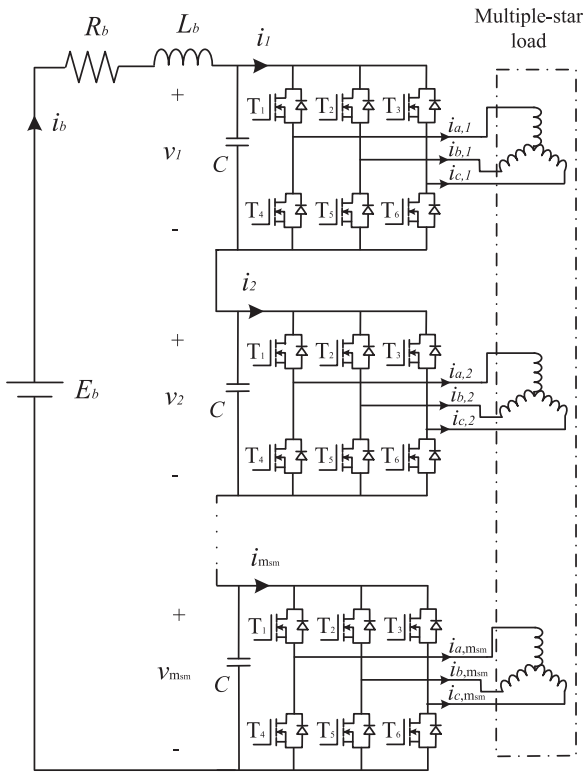

Fig. 1. SPB converter topology with m_{sm} submodules.

Since the capacitors are connected in series, the capacitor voltages need to be balanced in order not to give an uneven voltage stress on the submodules. In the motoring mode, balancing has to be made by means of control, as will shortly be shown. In [6] (as well as in [10], [13]–[15] for related topologies), such balancing is discussed. In [6], it is demonstrated that an active stabilization can be realized by adding increments to the current-component references of each converter submodule. In [7] and [8], dc-link controllers are designed and evaluated.

Despite this research effort, a comprehensive analysis of the open- and closed-loop SPB dynamics for an arbitrary number of submodules m_{sm} has, to the best knowledge of the authors, so far been lacking. The aim of this paper is to fill that void. The contributions and outline of this paper are as follows. In Section II, a dynamic model for the SPB converter is derived and its open-loop stability properties are studied. Thereafter, detailed designs and analyses of three alternatives of a balancing controller are made. The benefits and drawbacks of the three alternatives are clarified. Experimental and simulation results

are presented in Section III. In addition, the impact of a non-negligible submodule-to-submodule communication time delay is studied in Section III. Finally, a conclusion is reported in Section IV.

II. Analysis and Balancing-Controller Design

The SPB converter is depicted in Fig. 1. It is equipped with $m_{\rm sm}$ series-connected submodules. Each submodule (generally) consists of low-voltage components that are not able to sustain the full voltage E_b. Therefore, it is of essence that the voltage E_b is equally shared between the individual submodule capacitors, i.e., the submodule capacitor voltages should be balanced.

In this section, a dynamic model for the SPB converter with $m_{\rm sm}$ submodules is derived. Then, open-loop stability analyses for the SPB converter with, first one submodule, and thereafter, several submodules, are presented. This is followed by the introduction of three different alternatives for the balancing-controller design together with their closed-loop system stability analysis.

A. Dynamic Model

A model representing the capacitor-voltage dynamics for all submodules is first derived. From Fig. 1, we have

$$L_b\frac{di_b}{dt} = E_b - R_b i_b - \sum_{k=1}^{m_{\rm sm}} v_k \tag{1}$$

where E_b, i_b, L_b, and R_b are voltage, current, inductance, and resistance of the voltage source, respectively, and v_k is the voltage across each submodule capacitor ($k = 1, 2, \ldots, m_{\rm sm}$). It is expected that the inherent inductance in the conductors that connect the voltage source to the converter will suffice; thus, L_b is typically small, in the range of microhenries. All submodule capacitors are assumed to have the same capacitance C. For the kth capacitor voltage, with i_k as the current into the kth converter submodule, we have

$$C\frac{dv_k}{dt} = i_b - i_k. \tag{2}$$

If the converter losses of each submodule can be neglected, then i_k can be expressed as

$$i_k = \frac{P_k}{v_k} \tag{3}$$

where P_k is the power into the load (which is equal to the power into the kth converter submodule as well). Due to the nonlinear term P_k/v_k, (1)–(3) form a nonlinear system.

B. Open-Loop Stability

To start the analysis, the system (1)–(3) is expressed in state-space form with $\mathbf{x} = [i_b\ v_1\ v_2\ \ldots\ v_{m_{\rm sm}}]^T$. We obtain

$$\dot{\mathbf{x}} = \mathbf{f}(\mathbf{x}) \tag{4}$$

where

$$\mathbf{f}(\mathbf{x}) = \begin{bmatrix} (E_b - R_b i_b - \sum_{k=1}^{m_{\rm sm}} v_k)/L_b \\ (i_b - P_1/v_1)/C \\ (i_b - P_2/v_2)/C \\ \vdots \\ (i_b - P_{m_{\rm sm}}/v_{m_{\rm sm}})/C \end{bmatrix}. \tag{5}$$

To linearize (4), operating points and deviation quantities, denoted, respectively, by the superscript $\star$ and the prefix Δ, are introduced. As the aim is that each submodule should get an equal voltage share, it is assumed that all submodules have the same active-power operating point, i.e., $P_1^\star = P_2^\star = \cdots = P_{m_{\rm sm}}^\star = P^\star$. This gives $i_b = i_b^\star + \Delta i_b$, $v_k = v^\star + \Delta v_k$, and $P_k = P^\star + \Delta P_k$. Substituting these identities for i_b, v_k, and P_k into (4), we get the following two relations for the operating points:

$$v^\star = \frac{E_b - R_b i_b^\star}{m_{\rm sm}} \approx \frac{E_b}{m_{\rm sm}} \tag{6}$$

$$i_b^\star = \frac{P^\star}{v^\star} \tag{7}$$

where $R_b i_b^\star \ll E_b$ is used in the approximation in (6). By substituting $v_k = v^\star + \Delta v_k$ and $P_k = P^\star + \Delta P_k$ into the nonlinear relation P_k/v_k, it can be linearized as

$$\begin{aligned}\frac{P_k}{v_k} &= \frac{P^\star + \Delta P_k}{v^\star + \Delta v_k} = \frac{P^\star + \Delta P_k}{v^\star(1 + \Delta v_k/v^\star)} \\ &\approx \frac{(P^\star + \Delta P_k)(1 - \Delta v_k/v^\star)}{v^\star} \\ &\approx \frac{P^\star + \Delta P_k - P^\star \Delta v_k/v^\star}{v^\star}.\end{aligned} \tag{8}$$

Now, (8) is substituted into (4). This gives a linear state-space model

$$\dot{\Delta\mathbf{x}} = \mathbf{A}\Delta\mathbf{x} + \mathbf{B}\Delta\mathbf{u} \tag{9}$$

where

$$\begin{aligned}\Delta\mathbf{x} &= [\Delta i_b\ \Delta v_1\ \Delta v_2\ \cdots\ \Delta v_{m_{\rm sm}}]^T \\ \Delta\mathbf{u} &= [\Delta P_1\ \Delta P_2\ \cdots\ \Delta P_{m_{\rm sm}}]^T.\end{aligned} \tag{10}$$

The $(m_{\rm sm}+1) \times (m_{\rm sm}+1)$ matrix $\mathbf{A}$ and the $(m_{\rm sm}+1) \times m_{\rm sm}$ matrix $\mathbf{B}$ are given as

$$\mathbf{A} = \begin{bmatrix} -\frac{R_b}{L_b} & -\frac{1}{L_b} & \cdots & -\frac{1}{L_b} \\ \frac{1}{C} & \frac{P^\star}{Cv^{\star 2}} & \cdots & 0 \\ \vdots & \vdots & \ddots & \vdots \\ \frac{1}{C} & 0 & \cdots & \frac{P^\star}{Cv^{\star 2}} \end{bmatrix} \tag{11}$$

$$\mathbf{B} = \begin{bmatrix} 0 & 0 & \cdots & 0 \\ -\dfrac{1}{Cv^\star} & 0 & \cdots & 0 \\ 0 & -\dfrac{1}{Cv^\star} & \cdots & 0 \\ \vdots & \vdots & \ddots & \vdots \\ 0 & 0 & \cdots & -\dfrac{1}{Cv^\star} \end{bmatrix}. \tag{12}$$

C. Open-Loop Stability for $m_{\rm sm} = 1$

For the special case $m_{\rm sm} = 1$, the topology is comprised of a single three-phase two-level converter. In (11), $\mathbf{A}$ reduces to

$$\mathbf{A} = \begin{bmatrix} -\dfrac{R_b}{L_b} & -\dfrac{1}{L_b} \\ \dfrac{1}{C} & \dfrac{P^\star}{Cv^{\star 2}} \end{bmatrix}. \tag{13}$$

Stability is recognized by the characteristic polynomial $c(s) = \det(s\mathbf{I} - \mathbf{A})$, which from (13) is found as

$$c(s) = s^2 + \left(\frac{R_b}{L_b} - \frac{P^\star}{Cv^{\star 2}}\right) s + \frac{1}{L_b C}\left(1 - \frac{P^\star R_b}{v^{\star 2}}\right). \tag{14}$$

Using the Routh–Hurwitz stability criterion, asymptotic stability is obtained when all coefficients of $c(s)$ are positive. For (14), this holds for

$$\frac{R_b}{L_b} - \frac{P^\star}{Cv^{\star 2}} > 0, \quad 1 - \frac{P^\star R_b}{v^{\star 2}} > 0. \tag{15}$$

If in (15), $P^\star < 0$, i.e., generating mode, stability is always maintained. However, if $P^\star > 0$, the stability criterion may not always be fulfilled. This case is studied in [16], where a method for closed-loop stabilization is proposed.

D. Open-Loop Stability for $m_{\rm sm} > 1$

The general case with $m_{\rm sm}$ number of submodules is now considered. From (11), the characteristic polynomial can be found as

$$c(s) = \left(s - \frac{P^\star}{Cv^{\star 2}}\right)^{m_{\rm sm}-1} \times \left[s^2 + \left(\frac{R_b}{L_b} - \frac{P^\star}{Cv^{\star 2}}\right) s + \frac{1}{L_b C}\left(m_{\rm sm} - \frac{P^\star R_b}{v^{\star 2}}\right)\right]. \tag{16}$$

This polynomial has a second-degree factor, of which (14) is a special case for $m_{\rm sm} = 1$. The coefficient for s in the second-degree factor of (16) may turn negative for $P^\star > 0$. This corresponds to an instability mode that affects all submodule voltages in a similar manner. This instability mode thus affects the *total dc-link stability* and gives exponentially growing oscillations of approximately the angular frequency

$$\sqrt{\frac{1}{L_b C}\left(m_{\rm sm} - \frac{P^\star R_b}{v^{\star 2}}\right)} \approx \sqrt{\frac{m_{\rm sm}}{L_b C}} \tag{17}$$

i.e., the natural angular resonant frequency of the circuit. In addition, there are $m_{\rm sm} - 1$ identical first-degree factors in (16), which give right-half-plane eigenvalues for $P^\star > 0$. These instability modes affect the *submodule dc-link stability*, i.e., the balancing of the individual capacitor voltages. Because the eigenvalues are located on the real axis, these instability modes are exponentially growing without oscillations.

It can be concluded that, for $m_{\rm sm} > 1$, the system is always unstable in the motoring mode and closed-loop stabilization (balancing) is necessary. On the other hand, in the generating mode, i.e., $P^\star < 0$, the open-loop system is asymptotically stable.

E. Power to the Load (Machine)

As shown in Fig. 1, each submodule is connected to one set of three-phase windings of the load. A permanent-magnet synchronous machine (PMSM) with identical parameters for each set of three-phase windings is considered here as load. For the design and analysis of the balancing controller, it is vital first to obtain a linearized expression for the active power to the load.

If the submodule converter losses are neglected, the input power of each submodule is equal to the input power of the corresponding set of three-phase windings. With this approximation, the input power to submodule k can be expressed as

$$P_k = \frac{3}{2K^2}\Big[R_s\left(i_{d,k}^2 + i_{q,k}^2\right) + \omega_e \psi_m i_{q,k} + \omega_e (L_d - L_q) i_{d,k} i_{q,k}\Big] \tag{18}$$

where $i_{d,k}$ and $i_{q,k}$, respectively, are the d- and q-direction current components of the kth winding, R_s is the stator resistance, ψ_m is permanent-magnet flux linkage, L_d and L_q, respectively, are the d- and q-direction inductances, ω_e is the electrical rotor speed, and K is the space-vector scaling constant ($K = 1$ gives the amplitude-invariant transformation often used in control of PMSM drives).

Remark 1. The PMSM model can account also for a synchronous reluctance machine by letting $\psi_m = 0$. With ψ_m as the rotor-flux linkage, it can account for a rotor-flux-oriented induction machine by letting $L_d = L_q = L_\sigma$, where L_σ is the total leakage inductance. By letting $\omega_e = 0$, it accounts for a resistive–inductive (RL) load.

Remark 2. Modular PMSM designs suitable for the SPB converter topology are considered in, e.g., [12].

Equation (18) is now linearized. This is made by expressing the current components as $i_{d,k} = i_{d0} + \Delta i_{d,k}$ and $i_{q,k} = i_{q0} + \Delta i_{q,k}$, where i_{d0} and i_{q0} are the nominal values about which the linearization is made, whereas $\Delta i_{d,k}$ and $\Delta i_{q,k}$ are deviation variables (increments from the nominal values). This yields

$$P = P^\star + \Delta P_k \tag{19}$$

where

$$P^\star = \frac{3}{2K^2}\Big[R_s\left(i_{d0}^2 + i_{q0}^2\right) + \omega_e \psi_m i_{q0} + \omega_e (L_d - L_q) i_{d0} i_{q0}\Big] \tag{20}$$

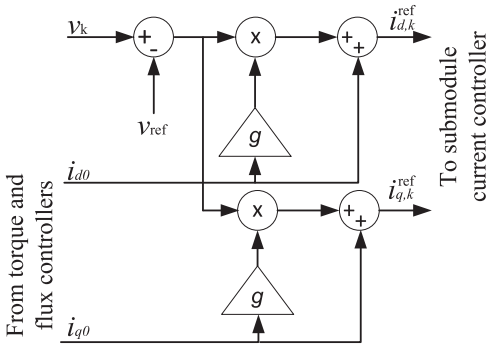

Fig. 2. Block diagram of the balancing controller.

and

$$\Delta P_k = \frac{3}{2K^2}\Big[\,2R_s(i_{d0}\Delta i_{d,k} + i_{q0}\Delta i_{q,k}) + \omega_e\psi_m\Delta i_{q,k} + \omega_e(L_d - L_q)(i_{d0}\Delta i_{q,k} + i_{q0}\Delta i_{d,k})\,\Big]. \tag{21}$$

F. Balancing-Controller Design

As found in Section II-D, the dynamics of the submodule capacitor voltages are open-loop unstable in the motoring mode and need closed-loop stabilization. We, therefore, in the following, use (21) to analyze the properties of three alternatives of a balancing controller. In all three alternatives, an individual stabilization term with a gain g is added to the current-component references $i_{d,k}^{\mathrm{ref}}$ and $i_{q,k}^{\mathrm{ref}}$ for submodule k. The stabilization terms for each submodule are made proportional to the individual voltage deviation from the reference voltage v_{ref}, as (see Fig. 2)

$$\begin{aligned} i_{d,k}^{\mathrm{ref}} &= i_{d0} + g i_{d0}(v_k - v_{\mathrm{ref}}) \\ i_{q,k}^{\mathrm{ref}} &= i_{q0} + g i_{q0}(v_k - v_{\mathrm{ref}}) \end{aligned} \tag{22}$$

where i_{d0} and i_{q0}, respectively, are set by the flux and torque controllers. These values are common for all submodules. Each submodule has a dedicated current controller, with $i_{d,k}^{\mathrm{ref}}$ and $i_{q,k}^{\mathrm{ref}}$ as inputs along with locally obtained machine stator-current measurements. Local measurement of v_k, with minimal time delay, is used as well. Finally, the definition of v_{ref} is

$$v_{\mathrm{ref}} = \begin{cases} v_\Sigma/m_{\mathrm{sm}}, & \text{for controller alternative I} \\ E_b/m_{\mathrm{sm}}, & \text{for controller alternative II} \\ v_{\Sigma f}/m_{\mathrm{sm}}, & \text{for controller alternative III} \end{cases} \tag{23}$$

where $v_\Sigma = \sum_{k=1}^{m_{\mathrm{sm}}} v_k$ and $v_{\Sigma f}$ is a low-pass filtered variant of v_Σ. The details for these controller alternatives are presented in the following.

1) Controller Alternative I: This controller alternative was previously proposed in [17]. It is an extension of the controller presented in [16] that accounts for the modular nature of the SPB converter topology.

Assuming that the current control is made with high accuracy and bandwidth so that $i_{d,k} = i_{d,k}^{\mathrm{ref}}$ and $i_{q,k} = i_{q,k}^{\mathrm{ref}}$ can be assumed, then $\Delta i_{d,k} = g i_{d0}(v_k - v_\Sigma/m_{\mathrm{sm}})$ and $\Delta i_{q,k} = g i_{q0}(v_k - v_\Sigma/m_{\mathrm{sm}})$. Substitution into (21) yields

$$\begin{aligned} \Delta P_k &= \frac{3}{2K^2}\Big[\,2R_s(i_{d0}^2 + i_{q0}^2) + \omega_e\psi_m i_{q0} \\ &\quad + 2\omega_e(L_d - L_q) i_{d0} i_{q0}\,\Big]\, g(v_k - v_\Sigma/m_{\mathrm{sm}}) \\ &= g'(v_k - v_\Sigma/m_{\mathrm{sm}}) \end{aligned} \tag{24}$$

where from (20), it follows that:

$$g' = g\left(2P^\star - \frac{3\omega_e\psi_m i_{q0}}{2K^2}\right). \tag{25}$$

The impact of (24) on the system stability can be analyzed in two steps. First, the dynamics of the second-order system that is formed by state variables i_b and v_Σ, i.e., the total dc-link stability, is considered. Thereafter, the dynamics of the individual voltages v_k are considered, i.e., the submodule dc-link stability. To this end, $v_\Sigma = \sum_{k=1}^{m_{\mathrm{sm}}} v_k$ is introduced in (1), and (2) is summed from $k = 1$ to $k = m_{\mathrm{sm}}$, giving

$$L_b\frac{di_b}{dt} = E_b - R_b i_b - v_\Sigma \tag{26}$$

$$\begin{aligned} C\frac{dv_\Sigma}{dt} &= m_{\mathrm{sm}} i_b - \sum_{k=1}^{m_{\mathrm{sm}}} i_k \\ &= m_{\mathrm{sm}} i_b - \sum_{k=1}^{m_{\mathrm{sm}}} \frac{P_k}{v_k}. \end{aligned} \tag{27}$$

Equations (26) and (27) are linearized using (8) as

$$L_b\frac{d\Delta i_b}{dt} = -R_b\Delta i_b - \Delta v_\Sigma \tag{28}$$

$$\begin{aligned} C\frac{d\Delta v_\Sigma}{dt} &= m_{\mathrm{sm}}\Delta i_b - \sum_{k=1}^{m_{\mathrm{sm}}} \frac{\Delta P_k - P^\star\Delta v_k/v^\star}{v^\star} \\ &= m_{\mathrm{sm}}\Delta i_b + \frac{P^\star\Delta v_\Sigma}{v^{\star 2}} - \sum_{k=1}^{m_{\mathrm{sm}}}\frac{\Delta P_k}{v^\star} \end{aligned} \tag{29}$$

where $\Delta v_\Sigma = \sum_{k=1}^{m_{\mathrm{sm}}} \Delta v_k$. Substituting (24) into (29) yields

$$C\frac{d\Delta v_\Sigma}{dt} = m_{\mathrm{sm}}\Delta i_b + \frac{P^\star\Delta v_\Sigma}{v^{\star 2}} - \underbrace{\sum_{k=1}^{m_{\mathrm{sm}}}\frac{g'(v_k - v_\Sigma/m_{\mathrm{sm}})}{v^\star}}_{0}. \tag{30}$$

Because the terms in (30) that are proportional to g' sum up to zero, the characteristic polynomial of (28) and (30) is identical to the second-degree factor of (16), i.e.

$$s^2 + \left(\frac{R_b}{L_b} - \frac{P^\star}{Cv^{\star 2}}\right)s + \frac{1}{L_b C}\left(m_{\mathrm{sm}} - \frac{P^\star R_b}{v^{\star 2}}\right). \tag{31}$$

Total dc-link stability, i.e., asymptotic stability of the system (28) and (30), is achieved when all the coefficients of the characteristic polynomial are positive. This means that the following inequalities must hold:

$$\frac{R_b}{L_b} - \frac{P^\star}{Cv^{\star 2}} > 0, \qquad m_{\mathrm{sm}} - \frac{P^\star R_b}{v^{\star 2}} > 0. \tag{32}$$

The right-hand inequality usually holds, because R_b is generally small. On the other hand, a small R_b may cause a problem in the left-hand inequality. A sufficiently large capacitance is needed for the left-hand inequality to hold, i.e.

$$C > \frac{P^\star L_b}{v^{\star 2} R_b}. \tag{33}$$

It can be noted that a small inductance L_b (i.e., the inherent source inductance) is beneficial, as it permits a smaller capacitance.

The submodule dc-link stability, i.e., the dynamics of the individual capacitor voltages v_k, $k = 1, 2, \ldots, m_{\rm sm}$, is now considered. Substituting (8) into (2) yields the linearized equation

$$C\frac{d\Delta v_k}{dt} = \Delta i_b - \frac{\Delta P_k - P^\star \Delta v_k / v^\star}{v^\star}. \tag{34}$$

Further, substituting (24) into (34) gives

$$C\frac{d\Delta v_k}{dt} = \Delta i_b - \frac{g' - P^\star/v^\star}{v^\star}\Delta v_k + \frac{g'}{m_{\rm sm} v^\star}\Delta v_\Sigma. \tag{35}$$

The variables Δi_b and Δv_Σ, which act as input signals to (35), come from the total dc-link subsystem, i.e., (28) and (30). This subsystem, which is asymptotically stable provided that (33) is fulfilled, on the other hand does not have Δv_k, $k = 1, 2, \ldots, m_{\rm sm}$, as explicit input signals. That is, the total dc-link subsystem feeds into the submodule dc-link subsystems, but not vice versa; a closed loop is not formed. Consequently, (35) is asymptotically stable when

$$g' > \frac{P^\star}{v^\star}. \tag{36}$$

Let us express this stability condition in g. For this purpose, it is convenient to express g in the dimensionless parameter γ, as follows:

$$g = \frac{\gamma}{v^\star} \approx \gamma \frac{m_{\rm sm}}{E_b}. \tag{37}$$

Using (25), this parameterization allows the condition $g' > P^\star/v^\star$ to be expressed as

$$\gamma > \frac{P^\star}{2P^\star - 3\omega_e \psi_m i_{q0}/(2K^2)}. \tag{38}$$

Here, two special cases can be identified:

1) for a machine load with negligible reluctance torque and negligible losses, $P^\star \approx 3\omega_e \psi_m i_{q0}/(2K^2)$, we get $\gamma > 1$;
2) for an RL load, we have $\psi_m = 0$, giving $\gamma > 0.5$.

2) Controller Alternative II: For the controller alternative I, the minimum capacitance requirement (33) must be observed in order to obtain stability. This may be a drawback. Even if a smaller capacitance than (33) would be sufficient from other aspects, such as harmonics, still a larger capacitance is required to maintain stability. As will shortly be shown, the controller alternative II does not have that drawback. Since $v^\star \approx E_b/m_{\rm sm}$, (22) with $v_{\rm ref} = E_b/m_{\rm sm}$ can be expressed as

$$\begin{aligned} i_{d,k}^{\rm ref} &= i_{d0} + g i_{d0} \Delta v_k \\ i_{q,k}^{\rm ref} &= i_{q0} + g i_{q0} \Delta v_k \end{aligned} \tag{39}$$

where $\Delta v_k \approx v_k - E_b/m_{\rm sm}$. Again assuming that the current control is made with high accuracy and bandwidth so that $i_{d,k} = i_{d,k}^{\rm ref}$ and $i_{q,k} = i_{q,k}^{\rm ref}$, then $\Delta i_{d,k} = g i_{d0} \Delta v_k$ and $\Delta i_{q,k} = g i_{q0} \Delta v_k$. Substitution into (21) yields

$$\begin{aligned} \Delta P_k &= \frac{3}{2K^2}\Big[\, 2R_s({i_{d0}}^2 + {i_{q0}}^2) + \omega_e \psi_m i_{q0} \\ &\quad + 2\omega_e (L_d - L_q) i_{d0} i_{q0} \,\Big]\, g \Delta v_k \\ &= g' \Delta v_k \end{aligned} \tag{40}$$

where g' is given by (25). The total dc-link stability properties that result from the controller alternative II are analyzed by substituting (40) into (29). Together with (28), this yields

$$L_b \frac{d\Delta i_b}{dt} = -R_b \Delta i_b - \Delta v_\Sigma \tag{41}$$

$$C\frac{d\Delta v_\Sigma}{dt} = m_{\rm sm}\Delta i_b + \frac{P^\star \Delta v_\Sigma}{v^{\star 2}} - \underbrace{\sum_{k=1}^{m_{\rm sm}} \frac{g' \Delta v_k}{v^\star}}_{g' \Delta v_\Sigma / v^\star}. \tag{42}$$

The characteristic polynomial of (41) and (42) is given by

$$s^2 + \left(\frac{R_b}{L_b} - \frac{P^\star - g' v^\star}{C v^{\star 2}}\right) s + \frac{1}{L_b C}\left[m_{\rm sm} - \frac{R_b (P^\star - g' v^\star)}{v^{\star 2}}\right]. \tag{43}$$

This is different from the characteristic polynomial (31) that results from the controller alternative I in the sense that terms proportional to g' are present. That is, the balancing controller affects also the total dc-link stability. Asymptotic stability of the system (41) and (42) is achieved when the coefficients of (43) are positive, i.e., for

$$\frac{R_b}{L_b} - \frac{P^\star - g' v^\star}{C v^{\star 2}} > 0, \qquad m_{\rm sm} - \frac{R_b (P^\star - g' v^\star)}{v^{\star 2}} > 0. \tag{44}$$

The right-hand inequality usually holds, because R_b is generally small. On the other hand, a small R_b may cause a problem in the left-hand inequality. A sufficiently large g' is needed for the first inequality to hold, i.e.

$$g' > \frac{P^\star L_b - v^{\star 2} R_b C}{L_b v^\star} \approx \frac{P^\star}{v^\star}. \tag{45}$$

With the approximation, this is the same stability condition as (36) for the submodule dc-link stability of the controller alternative I. The submodule dc-link stability properties for the controller alternative II can be shown to be the same as for the controller alternative I. Consequently, both total and submodule dc-link stability is obtained provided that (36) is fulfilled, irrespective of the dc-link capacitance C. It should be noted that $v^\star \approx E_b/m_{\rm sm}$ is used in the control law, which implies that E_b needs to be measured. This is the drawback of the controller alternative II.

3) Controller Alternative III: The benefit of the controller alternative I, i.e., avoidance of measurement of E_b, can be combined with the benefit of the controller alternative II, i.e., no minimum value for the dc-link capacitance. This is achieved

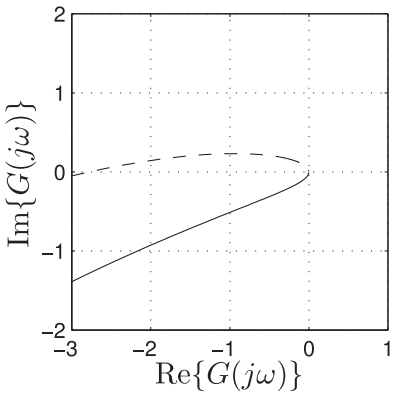

Fig. 3. Nyquist curves for (solid) the controller alternative III and (dashed) controller alternative I.

by letting $v_{\rm ref} = v_{\Sigma f}/m_{\rm sm}$ in (22), where $v_{\Sigma f} = H(s)v_\Sigma$ and $H(s)$ is a low-pass-filter transfer function in the differential operator $s = d/dt$.

A first-order filter $H(s) = \alpha_f/(s+\alpha_f)$ is adequate. If the bandwidth α_f is made significantly lower than the angular resonant frequency of the circuit, i.e., $\alpha_f \ll \sqrt{m_{\rm sm}/(L_b C)}$, then resonant-frequency oscillations will be suppressed and $v_{\Sigma f} \approx E_b$. That is, the controller alternative III has dynamic properties similar to the controller alternative II. This alternative is useful in situations where it is desired to have a capacitance smaller than that given by (33) while measurement of E_b is not feasible.

The submodule dc-link stability properties resulting from the controller alternative III can be shown to be the same as for the controller alternative I. The total dc-link stability properties can, as previously, be analyzed via a linearized second-order subsystem comprising the state variables Δi_b and Δv_Σ

$$L_b \frac{d\Delta i_b}{dt} = -R_b \Delta i_b - \Delta v_\Sigma \tag{46}$$

$$C\frac{d\Delta v_\Sigma}{dt} = m_{\rm sm}\Delta i_b + \frac{P^\star \Delta v_\Sigma}{v^{\star 2}} - \frac{g'}{v^\star}[1-H(s)]\Delta v_\Sigma. \tag{47}$$

Equations (46) and (47) can equivalently be expressed as the negative-feedback system

$$\Delta v_\Sigma = -G(s)\Delta v_\Sigma \tag{48}$$

where

$$G(s) = \frac{1}{sC}\left\{\frac{1}{sL_b + R_b} - \frac{P^\star}{v^{\star 2}} + \frac{g'}{v^\star}[1-H(s)]\right\}. \tag{49}$$

The stability of (46) and (47) can, thus, be analyzed by applying the Nyquist criterion to (49). Let us, as an example, consider a system with the parameters $m_{\rm sm} = 4$, $L_b = 2$ mH, $R_b = 1.15\ \Omega$, $C = 100\ \mu$F, $P^\star = 100$ W, $v^\star = 25$ V, $\omega_e = 0$, and $\gamma = 1$. For these parameters, (33) does not hold, i.e., the controller alternative I would give instability. The solid Nyquist curve in Fig. 3 is that obtained for the controller alternative III with $H(s) = \alpha_f/(s+\alpha_f)$ and $\alpha_f = 0.1\sqrt{m_{\rm sm}/(L_b C)}$. It does not encircle -1, so stability is obtained. On the other hand, the dashed Nyquist curve, which is obtained for $H(s) = 1$, i.e., for the controller alternative I, encircles -1.

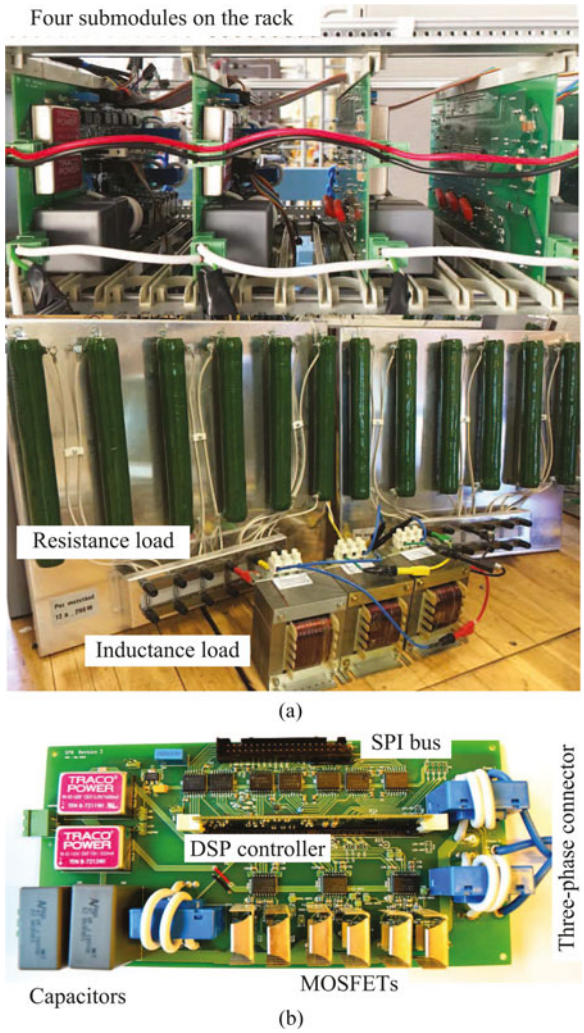

Fig. 4. Experimental setup: (a) SPB converter with four submodules connected to an RL load. (b) One submodule structure.

III. Experimental and Simulation Results

The experimental setup that is shown in Fig. 4(a) comprises an SPB converter with $m_{\rm sm} = 4$ submodules, where each phase leg of every submodule is connected to an individual RL load. Each submodule is constructed on a printed circuit board (PCB); see Fig. 4(b). Voltage E_b is supplied by a variable dc voltage source.

Each submodule is designed as a 100-V, 20-A, two-level, three-phase converter with a dc-link capacitor of $C = 100\ \mu$F. The capacitors are film type and surface mounted. The source inductance is very small, $L_b \approx 8\ \mu$H, whereas $R_b \approx 0.35\ \Omega$. Consequently, (33) for the controller alternative I is fulfilled. Each PCB has one digital signal processor (DSP)—of type TMS320F2806x MCUs—to control the switching signals and to handle the communication. The serial peripheral interface (SPI) bus protocol is chosen for the communication. The

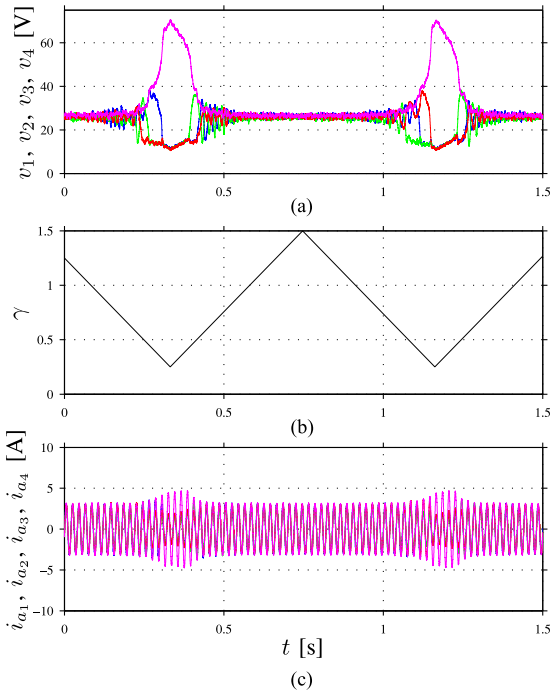

Fig. 5. Experimental results for the controller alternative I, submodule dc-link stability. (a) Submodule capacitor voltages. (b) Variation of γ. (c) One phase current ($i_{a,k}$) of each submodule.

information between the four submodules (e.g., dc-link voltages) is transmitted through the SPI bus that is coupled to the DSP. One submodule operates as master and the others operate as slaves. In addition, the switches are MOSFETs with a 20-kHz switching frequency. Finally, there are three current sensors on each PCB to measure the phase currents and the dc-link current.

All the submodules are designed so that they can operate as both master and slave. In the case of a fault on the master submodule, one of the slaves can switch to operate as master. In the other words, the control system has the potential to be fault tolerant.

Remark 3. In the case of a fault on one submodule, that submodule must be short circuited because of the series connection. (The submodules thus must have a voltage rating sufficient to withstand the increased voltage when changing from $m_{\rm sm}$ to $m_{\rm sm}-1$ series-connected submodules.) To safely create this short circuit is difficult and will be studied further in future research.

A. Submodule DC-Link Stability

To start with, the submodule dc-link stability is examined regarding the criterion (38). As explained in Section II-F1—since there is an RL load—for $\gamma < 0.5$, submodule dc-link stability is lost, whereas for $\gamma > 0.5$ asymptotic stable is obtained. This is verified by ramping γ up and down between the extreme values 0.25 and 1.5. The result shown in Fig. 5 agrees well with the theory.

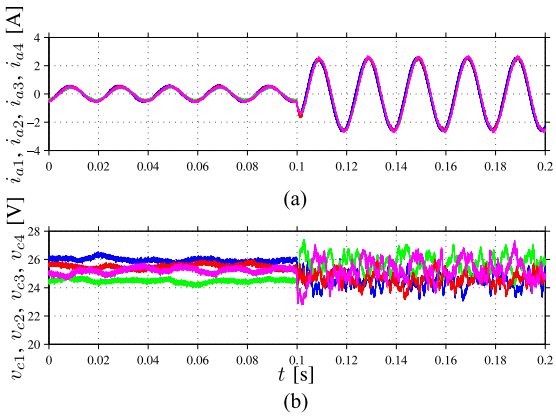

Fig. 6. Experimental results for the controller alternative I, total dc-link stability. (a) Submodule phase currents. (b) Submodule capacitor voltages.

B. Total DC-Link Stability

In order to violate the stability condition (33) for the controller alternative I, testing its practical validity, a relatively large air-core inductor, with a 2-mH inductance and a 0.8-Ω inner resistance, is installed in series with the inherent inductance of the source, giving $L_b \approx 2$ mH and $R_b \approx 1.15\ \Omega$. Together with $P^\star = 100$ W and $v^\star = 25$ V, (33) gives a minimum capacitance of 278 μF for stability. Since $C = 100$ μF, an unstable system would be expected.

Experimental results with the controller alternative I are shown in Fig. 6. For $t < 0.1$ s, the stability condition (33) holds. At $t = 0.1$ s, the current is increased and (33) is violated. Thus, instability would be expected for $t > 0.1$ s, but as can be seen, the system yet remains stable. (The steady-state deviations that can be seen in Fig. 6(b) are due to slight individual differences between the submodule components.)

The reason for the better result than expected of the controller alternative I may be somewhat surprising. There is a relatively large time delay $T_d \approx 0.5$ ms in the SPI communication between the submodules. This time delay can be modeled as the controller alternative III with $H(s) = e^{-sT_d}$. Similarly to the situation when $H(s)$ is chosen as a low-pass filter, the time delay improves the total dc-link stability properties. This claim will now be verified.

The system is simulated with the same parameters as in the experiment. In addition, switch-over to controller alternative III with $H(s) = \alpha_f/(s+\alpha_f)$, $\alpha_f = 400$ rad/s, is made at $t = 0.15$ s. The results are shown in Figs. 7 and 8, without and with time delay, respectively. As can be seen, the system without time delay turns unstable at $t = 0.1$ s (growing oscillations of the natural resonant frequency appear), but it regains stability when the controller alternative III is switched in. The system with time delay is stable for all the operating conditions.

In addition, verification can be made by applying the Nyquist criterion to (49) for, respectively, $H(s) = e^{-sT_d}$ and $H(s) = 1$. As Fig. 9 shows, the Nyquist curve in the system with time delay does not encircle -1.

Finally, Fig. 10 shows the correspondence to Fig. 6 for the controller alternative II. For unrelated reasons, the power supply

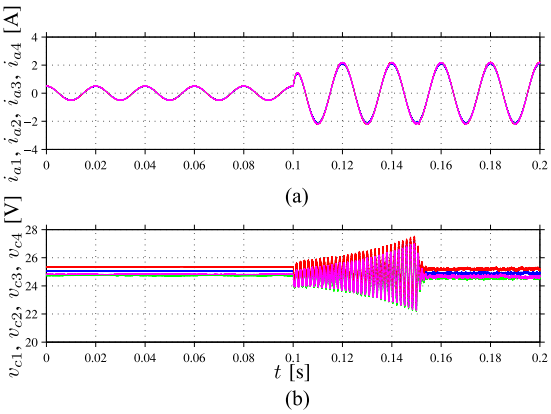

Fig. 7. Simulation results for the controller alternatives I ($t < 0.15$ s) and III ($t > 0.15$ s) without time delay, total dc-link stability. (a) Submodule phase currents. (b) Submodule capacitor voltages.

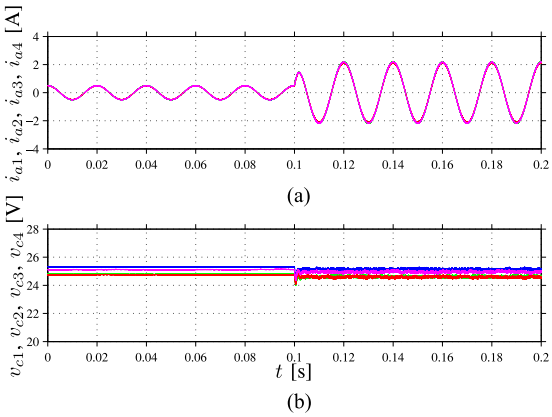

Fig. 8. Simulation results for the controller alternatives I ($t < 0.15$ s) and III ($t > 0.15$ s) with time delay, total dc-link stability. (a) Submodule phase currents. (b) Submodule capacitor voltages.

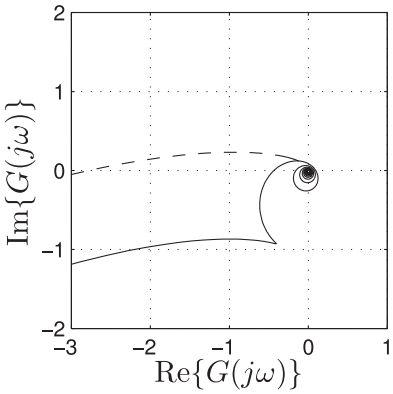

Fig. 9. Nyquist curves for the controller alternative I (solid) with and (dashed) without time delay.

is in this case a six-pulse diode rectifier. Due to its commutation voltage drop, all submodule voltages reduce following the power increase that occurs at $t = 0.1$ s. Otherwise, the results are very similar to Fig. 6. The system is stable, as predicted by the theory.

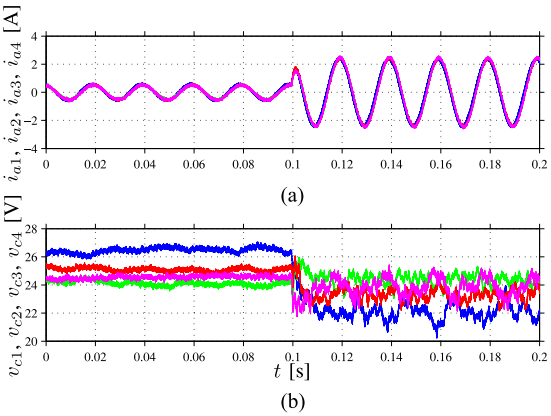

Fig. 10. Experimental results for the controller alternative II, total dc-link stability. (a) Submodule phase currents. (b) Submodule capacitor voltages.

IV. Conclusion

This paper presented dc-link stability analyses and three alternatives for the balancing-controller design of the SPB converter. The controller alternative I, which was previously proposed in [17], was shown to have the drawback of a minimum capacitance requirement for stability. This drawback was eliminated in the controller alternative II, which on the other hand requires source-voltage measurement. Both drawbacks were eliminated in the controller alternative III.

Interestingly, the presence of a communication time delay was in the experimental evaluation shown to improve the stability properties of the controller alternative I, allowing a smaller capacitance than the theoretical minimum. It was shown how the stability impact of a time delay in the controller alternative I can be analyzed using the Nyquist criterion.

References

[1] J. Rodriguez, S. Bernet, B. Wu, J. Pontt, and S. Kouro, "Multilevel voltage-source-converter topologies for industrial medium-voltage drives," *IEEE Trans. Ind. Electron.*, vol. 54, no. 6, pp. 2930–2945, Dec. 2007.

[2] M. Islam, Y. Guo, and J. Zhu, "A high-frequency link multilevel cascaded medium-voltage converter for direct grid integration of renewable energy systems," *IEEE Trans. Power Electron.*, vol. 29, no. 8, pp. 4167–4182, Aug. 2014.

[3] Z. Zheng, K. Wang, L. Xu, and Y. Li, "A hybrid cascaded multilevel converter for battery energy management applied in electric vehicles," *IEEE Trans. Power Electron.*, vol. 29, no. 7, pp. 3537–3546, Jul. 2014.

[4] P. Brockerhoff, Y. Burkhardt, K. Egger, and H. Rauh, "Highly integrated drivetrain solution: Integration of motor, inverter and gearing," in *Proc. 4th Int. Elect. Drives Prod. Conf.*, Sep. 2014, pp. 1–6.

[5] S. Norrga, L. Jin, O. Wallmark, A. Mayer, and K. Ilves, "A novel inverter topology for compact EV and HEV drive systems," in *Proc. IEEE 39th Annu. Conf. Ind. Electron. Soc.*, Nov. 2013, pp. 6590–6595.

[6] Y. Han, "Design, modeling, and control of multilevel converter motor drive with modular design and split winding machine," in *Proc. IEEE 15th Workshop Control Model. Power Electron.*, Jun. 2014, pp. 1–10.

[7] S. Gjerde and T. Undeland, "Power conversion system for transformer-less offshore wind turbine," in *Proc. 14th Eur. Conf. Power Electron. Appl.*, Aug. 2011, pp. 1–10.

[8] S. Gjerde, P. Olsen, K. Ljokelsoy, and T. Undeland, "Control and fault handling in a modular series-connected converter for a transformerless 100 kV low-weight offshore wind turbine," *IEEE Trans. Ind. Appl.*, vol. 50, no. 2, pp. 1094–1105, Mar. 2014.

[9] M. Quraan, T. Yeo, and P. Tricoli, "Design and control of modular multilevel converters for battery electric vehicles," *IEEE Trans. Power Electron.*, vol. 31, no. 1, pp. 507–517, Jan. 2016.
[10] A. Mayer, C. Rolff, and R. Marquardt, "Control concept and stability considerations of the modular high frequency converter," in *Proc. 16th Eur. Conf. Power Electron. Appl.*, Aug. 2014, pp. 1–10.
[11] H. Plesko, J. Biela, J. Luomi, and J. Kolar, "Novel concepts for integrating the electric drive and auxiliary DC-DC converter for hybrid vehicles," *IEEE Trans. Power Electron.*, vol. 23, no. 6, pp. 3025–3034, Nov. 2008.
[12] H. Zhang, O. Wallmark, M. Leksell, S. Norrga, M. Harnefors, and L. Jin, "Machine design considerations for an MHF/SPB-converter based electric drive," in *Proc. IEEE 40th Annu. Conf. Ind. Electron. Soc.*, Oct. 2014, pp. 3849–3854.
[13] J. Kimball, J. Mossoba, and P. Krein, "A stabilizing, high-performance controller for input series-output parallel converters," *IEEE Trans. Power Electron.*, vol. 23, no. 3, pp. 1416–1427, May 2008.
[14] R. Ayyanar, R. Giri, and N. Mohan, "Active input-voltage and load-current sharing in input-series and output-parallel connected modular dc-dc converters using dynamic input-voltage reference scheme," *IEEE Trans. Power Electron.*, vol. 19, no. 6, pp. 1462–1473, Nov. 2004.
[15] Z. Zheng, Z. Gao, C. Gu, L. Xu, K. Wang, and Y. Li, "Stability and voltage balance control of a modular converter with multiwinding high-frequency transformer," *IEEE Trans. Power Electron.*, vol. 29, no. 8, pp. 4183–4194, Aug. 2014.
[16] K. Pietiläinen, L. Harnefors, A. Petersson, and H.-P. Nee, "DC-link stabilization and voltage sag ride-through of inverter drives," *IEEE Trans. Ind. Electron.*, vol. 53, no. 4, pp. 1261–1268, Jun. 2006.
[17] M. Nikouie Harnefors, L. Jin, L. Harnefors, O. Wallmark, M. Leksell, and S. Norrga, "Analysis of the dc-link stability for the stacked polyphase bridges converter," in *Proc. 17th Eur. Conf. Power Electron. Appl.*, Sep. 2015, pp. 1–6.

Mojgan Nikouie (S'14) received the B.Sc. degree in electronic engineering from Tehran Azad University, Tehran, Iran, in 2005, and the M.Sc. degree in electric power engineering from the Chalmers University of Technology, Göteborg, Sweden, in 2013. She is currently working toward the Ph.D. degree at the Department of Electric Power and Energy Systems, KTH Royal Institute of Technology, Stockholm, Sweden.

Her research interests include power electronics and control and analysis of electric machines and drives.

Oskar Wallmark (S'01–M'06) received the M.Sc. degree in engineering physics, in 2001, and the Ph.D. degree in electric power engineering, in 2006, both from the Chalmers University of Technology, Göteborg, Sweden, and the Docent degree from the KTH Royal Institute of Technology, Stockholm, Sweden, in 2015.

He is currently an Associate Professor at the Department of Electric Power and Energy Systems, KTH Royal Institute of Technology. His main research interests include control and analysis of electric drives with particular focus on automotive applications.

Lebing Jin (S'13) received the M.Sc. degree, in 2012, from Tsinghua University, Beijing, China. She is currently working toward the Ph.D. degree in the Department of Electric Power and Energy Systems, KTH Royal Institute of Technology, Stockholm, Sweden.

Her research interests include power electronics, control and modulation.

Lennart Harnefors (S'93–M'97–SM'07) received the M.Sc., Licentiate, and Ph.D. degrees in electrical engineering from the KTH Royal Institute of Technology, Stockholm, Sweden, in 1993, 1995, and 1997, respectively, and the Docent degree in industrial automation from Lund University, Lund, Sweden, in 2000.

Between 1994 and 2005, he was with Mälardalen University, Västerås, Sweden, from 2001 as a Professor. Between 2001 and 2005, he was, in addition, a part-time Visiting Professor of electrical drives with the Chalmers University of Technology, Göteborg, Sweden. Since 2005, he has been with ABB, where he is currently a Senior Principal Scientist at Corporate Research, Västerås. He is, in addition, a part-time Adjunct Professor of power electronics with the KTH Royal Institute of Technology. His research interests include analysis and control of power electronic systems, particularly grid-connected converters and ac drives.

Prof. Harnefors is an Associate Editor of the IEEE TRANSACTIONS ON INDUSTRIAL ELECTRONICS and of *IET Electric Power Applications.*

Hans-Peter Nee (S'91–M'96–SM'04) received the M.Sc., Licentiate, and Ph.D. degrees in electrical engineering from the KTH Royal Institute of Technology, Stockholm, Sweden, in 1987, 1992, and 1996, respectively.

In 1999, he became Professor of power electronics at the Department of Electric Power and Energy Systems, KTH Royal Institute of Technology. His research interests include power electronic converters, semiconductor components, and control aspects of utility applications, such as flexible ac transmission systems and high-voltage dc transmission, and variable-speed drives.

Prof. Nee is a member of the European Power Electronics and Drives Association, involved with the Executive Council and the International Scientific Committee. He is an Associate Editor of the IEEE TRANSACTIONS ON POWER ELECTRONICS.